RAPID COMMUNICATION

Magnetic Resonance in Medicine 00:00–00 (2017)

Susceptibility Tensor Imaging and Tractography of Collagen Fibrils in the Articular Cartilage

Hongjiang Wei,[1] Eric Gibbs,[2] Peida Zhao,[1] Nian Wang,[3] Gary P. Cofer,[3] Yuyao Zhang,[1] G. Allan Johnson,[3] and Chunlei Liu[1,4]*

Purpose: To investigate the B_0 orientation-dependent magnetic susceptibility of collagen fibrils within the articular cartilage and to determine whether susceptibility tensor imaging (STI) can detect the 3D collagen network within cartilage.

Methods: Multiecho gradient echo datasets (100-μm isotropic resolution) were acquired from fixed porcine articular cartilage specimens at 9.4 T. The susceptibility tensor was calculated using phase images acquired at 12 or 15 different orientations relative to B_0. The susceptibility anisotropy of the collagen fibril was quantified and diffusion tensor imaging (DTI) was compared against STI. 3D tractography was performed to visualize and track the collagen fibrils with DTI and STI.

Results: STI experiments showed the distinct and significant anisotropic magnetic susceptibility of collagen fibrils within the articular cartilage. STI can be used to measure and quantify susceptibility anisotropy maps. Furthermore, STI provides orientation information of the underlying collagen network via 3D tractography.

Conclusion: The findings of this study demonstrate that STI can characterize the orientation variation of collagen fibrils where diffusion anisotropy fails. We believe that STI could serve as a sensitive and noninvasive marker to study the collagen fibrils microstructure. **Magn Reson Med 000:000–000, 2017. © 2017 International Society for Magnetic Resonance in Medicine.**

Key words: diffusion tensor imaging (DTI); susceptibility tensor imaging (STI); magnetic susceptibility; magnetic susceptibility anisotropy; knee; collagen fibril; articular cartilage

INTRODUCTION

Articular cartilage is a thin layer that covers the end of bones in joints. It is a type of fine connective tissue composed primarily of water (65%–80% of total mass), a complex mesh of collagen (10%–20% of total cartilage mass), and proteoglycans (1). In normal adult human articular cartilage, the network of collagen fibrils consists of three distinct layers: the superficial zone, where the fibrils are mostly parallel to the cartilage surface; the middle zone, where the fibrils are relatively randomly distributed; and the deep zone, where the fibrils are mostly oriented perpendicular to the cartilage surface (2). In normal joints, this collagen network acts as the structural framework for tissue, providing the main source of tensile and shear strength. In diseased joints, the organization and arrangement of the collagen network is essential to the characterization of alterations in the extracellular matrix that relate to pathogenesis and osteoarthritis (3,4). Attempts have been made to image the collagen network using MRI. The relaxation parameters of collagen were well investigated with NMR a decade ago (5–9). Structural imaging such as diffusion-weighted imaging and diffusion tensor imaging (DTI) has been used to map the diffusion anisotropy (10,11) but rarely used to map the complex, three-dimensional (3D) collagen fibril tractography due to limited spatial resolution and relatively low signal-to-noise ratio (SNR).

An alternative approach is to use susceptibility to evaluate the collagen network. Quantitative susceptibility mapping (QSM) images correlate strongly with local tissue properties in various organs (12–18). More recently, QSM has been successfully applied to probe the highly organized microstructure of cartilage and evaluate its magnetic susceptibility at different depths (19,20). 3D QSM maps are derived from 2D or 3D gradient-recalled echo (GRE) sequences (21–23), which can be quickly acquired at high resolution, especially at ultrahigh field strengths. However, QSM assumes that the macroscopic susceptibility in an imaging voxel is isotropic (24,25). Over the past few years, susceptibility tensor imaging (STI) has been developed to quantify susceptibility anisotropy and provide a unique structural contrast (15,18,26–32). For example, in the brain, STI shows strong anisotropy in the white matter fiber bundles, which is attributed to the aligned lipid chains in the myelin sheath surrounding the white matter axons (29,33,34). In the kidney, STI shows strong susceptibility anisotropy and assesses the highly organized nephron tubular structure throughout the kidney (18). In the heart, STI detects the microstructure of myofiber in the mouse heart and agrees with diffusion tensor data (12,15,35). Similarly, we reasoned that STI would also quantify susceptibility anisotropy of cartilage and tract

[1]Department of Electrical Engineering and Computer Sciences, University of California, Berkeley, California, USA.

[2]Department of Biomedical Engineering, Duke University, Durham, North Carolina, USA.

[3]Center for In Vivo Microscopy, Duke University, Durham, North Carolina, USA.

[4]Helen Wills Neuroscience Institute, University of California, Berkeley, California, USA.

Grant sponsor: National Institutes of Health; Grant numbers: NIMH R01MH096979; NIBIB 5P41EB015897, and NIH 1S10OD010683.

*Correspondence to: Chunlei Liu, Ph.D., Department of Electrical Engineering and Computer Sciences, and Helen Wills Neuroscience Institute, University of California, Berkeley, 505 Cory Hall, Berkeley, CA 94720. E-mail: chunlei.liu@berkeley.edu

Received 4 June 2017; revised 24 July 2017; accepted 30 July 2017

DOI 10.1002/mrm.26882

Published online 00 Month 2017 in Wiley Online Library (wileyonlinelibrary.com).

its collagen network, since susceptibility anisotropy exists in cartilage (19).

In the present study, a multiecho GRE sequence was used to obtain STI data from two porcine articular cartilage specimens at 9.4 T. Phase images from 12 or 15 orientations with respect to the static B_0 field were obtained to map quantitative susceptibility values and quantify the susceptibility anisotropy of collagen in local cartilage regions. The apparent magnetic susceptibility was plotted as a function of rotation angle referenced to the normal of the articular surface. Furthermore, we investigated the 3D estimation of voxel-wise collagen fibril orientation based on the STI data and compared that with results from DTI data. Our results reveal the layer-specific architecture of the 3D collagen fibril network within the cartilage. This multilayer structure is confirmed by atomic-force microscopy (AFM). These results demonstrate the potential of STI to noninvasively study 3D collagen structure and overcome the practical limitations of current MRI techniques.

METHODS

Specimen Preparation and Fixation

All animal preparation protocols were approved by the Duke University Institutional Animal Care and Use Committee. Fresh samples of two porcine knee joints were obtained from a local abattoir. A piece of each articular cartilage was removed from the central femoral condyles using a surgical knife. The cartilage was immersed in 10% formalin overnight and then immersed in 10 mM phosphate buffered saline the next day. Cartilage was first fixed without contrast agent and scanned to acquire STI data while immersed in Galden (porfluoropolyether; Solvay Specialty Polymer, Bruxelles, Belgium) to provide a background susceptibility properties similar to that of water. After this imaging session, the cartilage was stained by immersion in a saline solution of 2.5 mM Prohance (gadoteridol; Bracco Diagnostics Inc., Princeton, NJ) to reduce the T_1 relaxation time. This allows for a much shorter repetition time (TR). This strategy is important for achieving high resolution in a relatively shorter acquisition time and improving SNR (36). The cartilage was then scanned to acquire contrast-enhanced DTI images.

MR Data Acquisition

The animal experiments were performed using a 9.4 T, 8.9 cm vertical bore Oxford magnet controlled by an Agilent Direct Drive (VNMRJ 4.0 console). Each cartilage specimen was firmly affixed in an 11-mm cylindrical polyethylene cartridge. The specimen cartridge was placed inside a sphere, allowing for an arbitrary specimen orientation inside the coil (15,18). Magnitude and phase data were acquired using a 3D GRE sequence with 15 echoes (echo time $TE_1/\Delta TE/TE_{15} = 10/2/38$ ms); other imaging parameters were TR = 150 ms, flip angle = 35°, matrix size = $150 \times 150 \times 150$, isotropic voxel size = 100 μm, total scan time per orientation = 40 min. The specimen was repositioned in a new orientation prior to every image acquisition. To assess the B_0 orientation-dependent magnetic susceptibility, 12 or 15 image orientations were acquired for each specimen. For example, the unit vectors of 12 orientations from one specimen are included in Supporting Figure S1 and Table S1.

DTI datasets were acquired using two spin-echo scans with $b = 0$ s/mm^2 and 16 diffusion-encoded spin-echo scans. The diffusion gradient pulses were half-sine shaped with a duration δ of 3 ms. To investigate the effects of varying diffusion time for detecting collagen fibrils with larger diameters or larger spaces in between neighboring fibrils, the time interval Δ between the start of the diffusion pulses was 4, 8, or 16 ms corresponding to the effective diffusion time ($\Delta - \delta/4$) of 3.25, 7.25, and 15.25 ms, respectively. A hard pulse was used for refocusing with a duration of 0.2 ms, and $b = 1500$ s/mm^2 (TR = 150 ms, TE = 7.8, 11.8, or 19.8 ms, matrix size = $128 \times 128 \times 128$, isotropic voxel size = 100 μm, total scan time = 8 h, 11 min).

Imaging Reconstruction and Processing

The raw k-space data from multiecho GRE acquisition was used to generate magnitude and phase images. Phase images were processed by Laplacian-based phase unwrapping (37) and V_SHARP background phase removal methods (23,38). The filtered phase images were normalized by TE and then averaged across echoes to produce the SNR-enhanced phase image. The magnitude images acquired at different orientations were first coregistered to a chosen reference orientation [B_0 vector = (0 0 1), 0° referenced to the normal of the articular surface] using rigid body transformation (FMRIB, Oxford University, UK, https://fsl.fmrib.ox.ac.uk/). The six rigid-body transformation parameters were estimated and then applied to SNR-enhanced phase images at different orientations. The 3D transformation matrices were used to calculate the rotation angles and $\hat{\mathbf{H}}$ vectors (i.e., unit vector along the applied main static field at the different orientations in the specimen frame of reference). Once all phase maps are processed, the susceptibility tensor $\boldsymbol{\chi}$ at each voxel was computed (30). There are six independent elements for a symmetric rank-2 susceptibility tensor, that is, χ_{11}, χ_{12}, χ_{13}, χ_{22}, χ_{23}, and χ_{33} from the nine-element tensor matrix. Eigenvalue decomposition was performed on the tensor to define the three principal susceptibility values (χ_1, χ_2, χ_3) with corresponding eigenvectors. The major eigenvector points in the direction with the most positive (paramagnetic) susceptibility and the minor eigenvector points were in the direction with the most negative (diamagnetic) susceptibility. The three eigenvalues were averaged to produce the mean magnetic susceptibility (MMS) image $\bar{\chi} = (\chi_1 + \chi_2 + \chi_3)/3$ (28), and the magnetic susceptibility anisotropy (MSA), $\Delta\chi = \chi_1 - (\chi_2 + \chi_3)/2$, was calculated at each voxel.

Comparison Between DTI and STI Tractography

To compare the DTI and STI, b0 image (DTI scan with b value = 0 s/mm^2) was registered to the one of the GRE magnitude images, then transformation matrices were applied to all diffusion-weighted images. Diffusion fractional anisotropy (FA) and mean diffusivity (MD) were

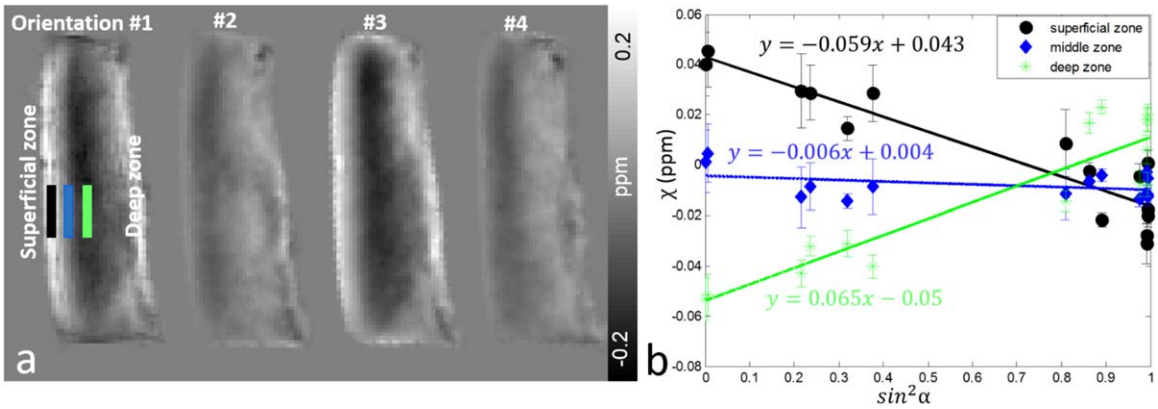

FIG. 1. (**a**) Apparent magnetic susceptibility maps measured at four out of 15 orientations. The magnetic susceptibility within the cartilage varies markedly from one orientation to another. (**b**) Plots of apparent magnetic susceptibility at different layers versus collagen fibril angle with respect to B_0 (black: superficial layer; blue: middle layer; green, deep layer). α was defined by the angle between the normal of the articular surface and B_0.

computed as described previously (39). DTI and STI tractography were performed using a streamline tracking algorithm developed for DTI (40). For STI, the vector fields were defined by the minor eigenvector. Both DTI and STI vector fields were propagated based on anisotropy measures and an angle threshold of 60° between neighboring voxels. Tracking was conducted using Diffusion Toolkit and TrackVis (http://www.trackvis.org/dtk/; Martinos Center for Biomedical Imaging, Massachusetts General Hospital, Boston, Massachusetts, USA).

Data Analysis

Regions of interest for quantitative analysis were defined at different depths within the cartilage using STISuite (University of California, Berkeley; https://people.eecs.berkeley.edu/~chunlei.liu/software.html). The mean apparent magnetic susceptibility within the regions of interest was calculated. Mean susceptibility values at different rotated orientations were plotted as a function of angle between the normal of the cartilage surface and the B_0 field. Susceptibility values were referenced to the mean susceptibility of the whole specimen.

Atomic-Force Microscopy

In its most basic setup, AFM is a characterization technique used to determine the surface topology of a variety of materials (41) and can specially be used to measure the collagen fibril orientation at high resolution (42,43). In this study, following MRI experiments, specimens were decalcified, paraffin-embedded, and sectioned serially into 5-μm-thick sections. Xylene was used to remove paraffin and unstained sections were mounted with DPX on glass slides as described previously (44). The articular cartilage topography was imaged by AFM (Dimension Icon from Bruker Corporation) at a scanning rate of ~0.7 Hz. Samples at different locations within the superficial zone, middle zone and deep zone were analyzed.

RESULTS

Figure 1a shows examples of apparent magnetic susceptibility (AMS) maps measured at four out of the 15 different orientations. The susceptibility maps exhibit local contrast specific to different cartilage layers. Moreover, the magnetic susceptibility maps clearly indicate an orientation dependency. Figure 1b plots AMS at different cartilage depths as a function of angle (α) between the normal of the cartilage surface and B_0. For example, at orientation #1 ($B_0 = [0\ 0\ 1]$), collagen fibrils are perpendicular and parallel to B_0 in the superficial zone and deep zone, respectively. Magnetic susceptibility is more paramagnetic when collagen fibrils are perpendicular to B_0 and are relatively more diamagnetic when fibrils are parallel to B_0. Specifically, the AMS displays a monotonic decrease in the superficial zone (in black, $y = -0.059 + 0.043$), a relatively constant value in the middle zone (in blue, $y = -0.006 + 0.004$) and a monotonic increase in the deep zone (in green, $y = 0.065 - 0.05$) (Fig. 1b). These findings suggest that there is a diamagnetic content in the collagen that points along the long axis and confirms that the STI eigenvector pointing along the collagen axis is the minor eigenvector (most diamagnetic). This result is consistent with a previous simulation study on a collagen model (19) and similar results are observed in the magnetic susceptibility of kidney tubules (18).

Figure 2 compares the susceptibility and diffusion tensors. There are dramatic visual and quantitative differences between the susceptibility and diffusion tensors. The susceptibility tensor provides higher image contrast than the diffusion tensor. Interestingly, they share similar cartilage layer patterns, as indicated by the white arrows. The susceptibility anisotropy inherent to the tensor is evident from the varying contrast between different tensor elements.

Examples of tensor eigenvalues, MD, FA, MMS, and MSA maps are shown in Figure 3. White arrows indicate the similarities shared by STI and DTI for detecting the cartilage layers. Red arrows point to the layers observed on STI and not on DTI. MSA values were 0.2 ± 0.02 ppm

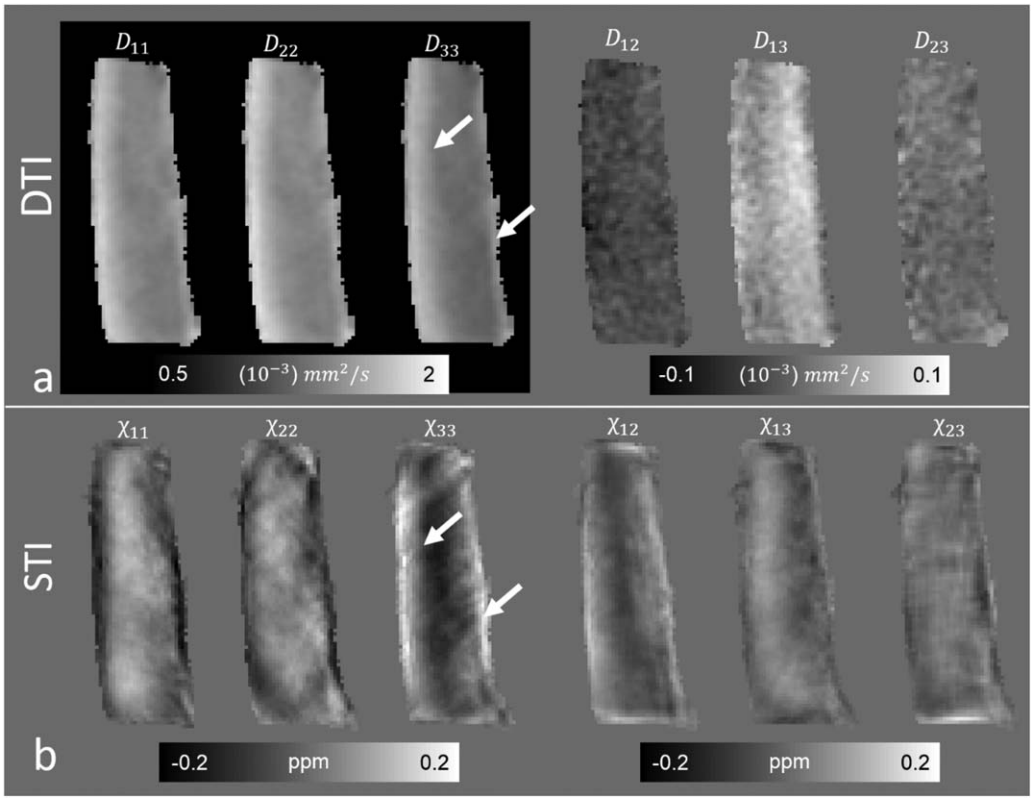

FIG. 2. Representative maps of susceptibility tensors and diffusion tensors. The arrows point to the similar layer pattern between STI and DTI. Obvious differences between STI and DTI can also be seen at different cartilage depths.

in the superficial zone, 0.05 ± 0.02 ppm in the middle zone and 0.16 ± 0.03 ppm in the deep zone. The MMS values in the corresponding zones were 0.04 ± 0.02 ppm, -0.02 ± 0.01 ppm and 0.02 ± 0.03 ppm, respectively. The mean diffusivity decreased from $1.7 \pm 0.2 \times 10^{-3}$ mm^2/s near the articular surface to $1.1 \pm 0.15 \times 10^{-3}$ mm^2/s at a depth of 50%–90% and finally increased to $1.5 \pm 0.12 \times 10^{-3}$ mm^2/s near the tide mark region. The absolute values of FA were relatively small increasing from 0.02 ± 0.02 near articular surface to 0.09 ± 0.03 at a depth of 50%–90%, and finally decreasing to 0.03 ± 0.02 near the tide mark. The MSA is further color-coded based on the direction of the eigenvector associated with the tertiary (most diamagnetic) susceptibility. The predominant orientation of the color-coded MSA is parallel to the cartilage surface in the superficial zone. Similarly, in a ribbon-like area close to the tidemark zone, a predominantly tangential alignment of the eigenvectors can be seen. In between these two regions, the predominant orientation of the eigenvectors is perpendicular to the cartilage surface. This area accounts for about 50%–60% of the total thickness of the cartilage. The difference between DTI and STI for measuring the collagen fibril orientation is also observed from tensor fields, as shown in Supporting Figure S2.

Finally, Figure 4 compares 3D fiber tracts of collagen fibrils reconstructed using DTI and STI. STI can characterize the orientation variation of collagen fibrils at different depths where DTI fails. Blue color shows where collagen fibrils are perpendicular to the cartilage surface while yellow and red show where collagen fibrils are parallel to the cartilage surface. A zoomed-in portion of the middle slice of cartilage better depicts the collagen fibril orientation, as shown from the white rectangle in Figure 4c. STI shows well-organized collagen fibril orientation in the deep zone and superficial zone. Similar magnetic susceptibility anisotropy and 3D collagen tracks are also observed in another specimen (Supporting Fig. S3).

The observed multilayer cartilage structure pattern and collagen fibril orientation (Fig. 5a) are verified by the AFM experiment. As shown in Figure 5b, the collagen fibril orientations (indicated by the double-headed arrows) are perpendicular and parallel to the cartilage surface in deep zone and superficial zone, respectively. Collagen fibrils are randomly distributed in the middle zone (Fig. 5b) and the net susceptibility anisotropy is close to zero. The fiber tracking algorithm stopped when the fiber angle is above the threshold, resulting in no visualized fiber in the middle zone, as shown in Figure 5a.

DISCUSSION

In this study, we assessed the ability of STI to analyze articular cartilage and investigated whether STI can probe regional structural properties of the collagen matrix. We first hypothesized that magnetic susceptibility anisotropy is a reliable marker of oriented ultrastructure of cartilage based on orientation-dependent magnetic susceptibility. We compared susceptibility measurements to diffusion

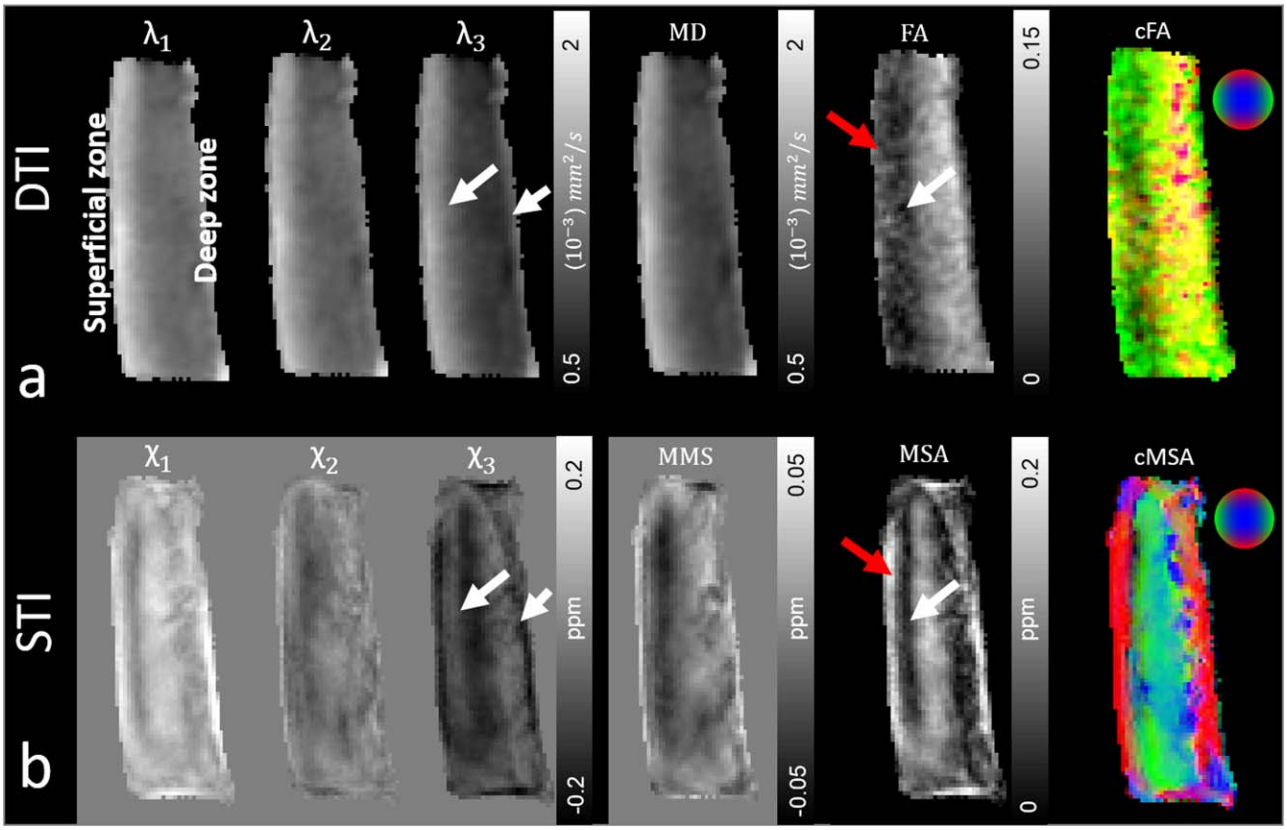

FIG. 3. Representative images of (**a**) diffusion tensor eigenvalues, MD, FA, color-coded diffusion anisotropy and (**b**) susceptibility tensor eigenvalues, mean magnetic susceptibility, susceptibility anisotropy, and color-coded magnetic susceptibility anisotropy. The color is defined by the eigenvector associated with the maximal principal diffusivity for DTI and minimal susceptibility for STI. Red, green, and blue colors represent the local orientation of the collagen fibril, which indicate up-down, left-right and anterior–posterior, respectively.

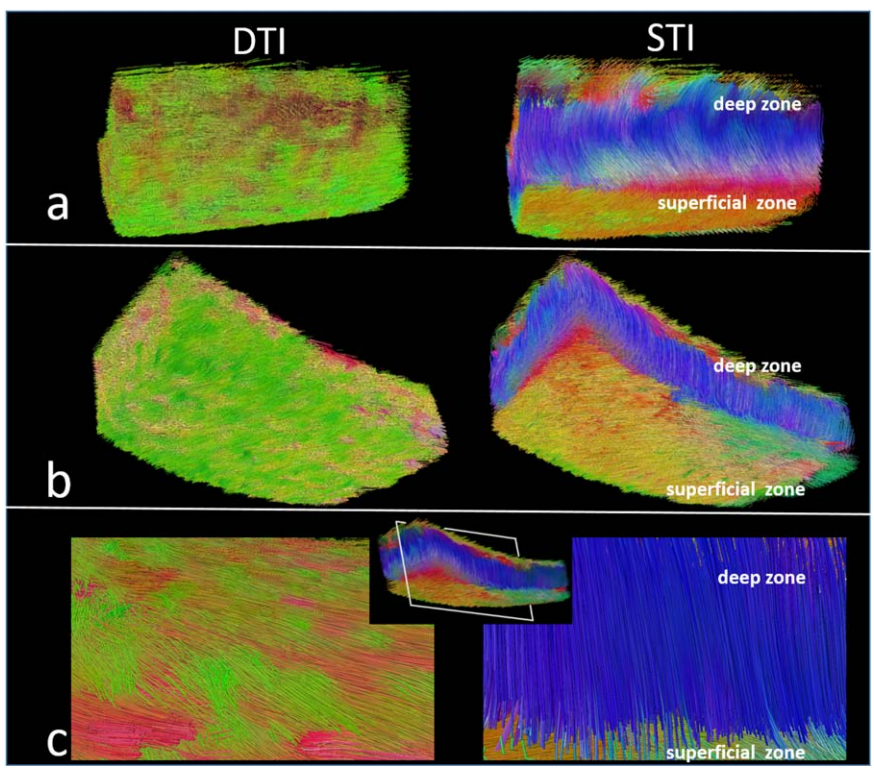

FIG. 4. Comparison of DTI and STI fiber tracts of collagen fibrils in 3D. STI can characterize the orientation variation of collagen fibrils at different cartilage depths where DTI fails. Blue color shows that collagen fibrils are perpendicular to the cartilage surface, while yellow and red colors show collagen fibrils that are parallel to the cartilage surface.

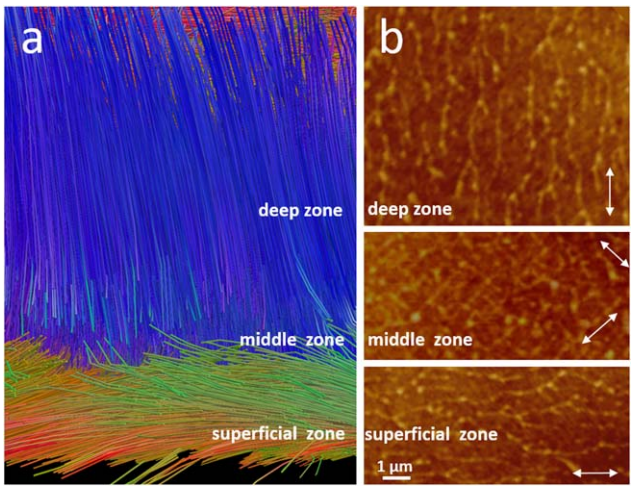

FIG. 5. (**a**) A zoomed-in view of the region illustrates fine collagen fibril structure in the deep zone, middle zone, and superficial zone of STI tracts. (**b**) AFM sections at different locations from the deep zone to superficial zone are shown for comparison. Collagen fibril directions are indicated by double-headed arrows in each layer.

measurements and concluded that susceptibility has a higher sensitivity to collagen fibril orientation as measured by tensor eigenvector orientations. We then used STI to achieve the first high-resolution 3D collagen fibril tractography with MRI. Finally, we confirmed the underlying collagen fibril layer structure by AFM.

Tensor Imaging Results Explained by the Collagen Fibril

Susceptibility anisotropy offers much higher sensitivity to the chemical composition of collagen fibril structure than diffusion anisotropy, thus confirming that DTI and STI anisotropy rely on an entirely different contrast mechanism.

In cartilage, the right-handed collagen-typical triple helix is ~1–1.5 nm in diameter (45). The staggered assembly of five triple helices yields a microfibril segment and 14 microfibrils make up a complete collagen fibril (~20–40 nm diameter) (46). The mature single collagen fiber in the cartilage is reported to have a diameter up to 200 nm. The fibril–fibril separation is reported to be a few hundred nanometers (47) and the space measured here using AFM is ~1 μm, as shown in Figure 5b. The mean diffusion distances of water molecular are determined via the Einstein equation, as $\sqrt{2Dt}$, where $t = \Delta - \delta/4$ is the effective diffusion time with half-sine-shaped gradient and D is the diffusion coefficient. For example, with measured mean diffusivity $\sim 1.7 \times 10^{-3}$ mm^2/s in the superficial zone, the mean diffusion displacement is ~5 μm and ~7.2 μm for the given diffusion times of 8 ms and 16 ms, respectively. With this time scale, we should be able to probe the microstructural boundaries of interest. However, as shown by the color-coded FA, low FA values and randomly distributed diffusion eigenvectors cannot probe the highly organized collagen fibrils well (Supporting Fig. S4). One explanation is that proteoglycans restrict water molecule diffusion. Proteoglycans consist of a protein core and highly charged anionic chains. These chains vertically align with collagen fibrils, occupying narrow spaces among neighboring parallel collagen fibrils and attract water molecules (48). As a result, the proteoglycans affect the diffusivity of water molecular within the interfibrillar spaces. Thus, we may conclude that DTI lacks the sensitivity of detecting the orientation of collagen fibril in the cartilage compared with STI.

The basic principle of STI tractography of a collagen fibril is that the magnetic susceptibility anisotropy lies along the collagen long axis. The macroscopic susceptibility anisotropy of collagen comes from the diamagnetic anisotropy of arranged peptide groups at the molecular level. Collagen in cartilage is a polypeptide chain rich in left-handed polyproline type II helices. These peptide group planes orient at approximately 45° to the fibril axis and have an out-of-plane susceptibility that is more diamagnetic than their in-plane susceptibility (49). Because the most diamagnetic susceptibility is oriented normal to the peptide group plane, the net susceptibility of collagen fibrils is most diamagnetic in the direction parallel to the fibril axis (49,50). This finding is consistent with the fact that the minor eigenvector of the susceptibility tensor is pointed along the collagen long axis. Note that this behavior of susceptibility anisotropy differs from that observed in brain white matter, in which myelinated axons appear more paramagnetic when parallel to the B_0 field.

Application and Future Directions

The characteristics of STI, such as high SNR, high spatial resolution, and the low specific-absorption rate of GRE scans, make it an attractive method for high resolution tensor imaging of in vivo human organs. However, STI requires rotating tissue at different angles with respect to the B_0 field. This is the major challenge for in vivo human cartilage STI scans due to the difficulties of knee rotation in clinical MRI scanners. Recently, a spectrum analysis of the multipole magnetic response or p-space MRI has been proposed to achieve susceptibility-based white matter fiber orientation determination without rotating the brain (51). In vivo human cartilage STI scans can also be achieved with novel design of open magnet by being capable of rotating the direction of the B_0 field (52). The practical utility of this promising approach for in vivo human articular cartilage imaging needs further investigation.

CONCLUSION

Our results indicate the feasibility and applicability of STI experiments to study collagen fibril orientation in the cartilage in high-field-strength MRI. MRI is a promising tool to understand the complex structures of cartilage because it is nondestructive, has the ability to assess the collagen network in 3D, and STI provides rich structural contrasts and quantitative analysis. More importantly, the potential of STI methods can answer critical questions about knee diseases related to the alignment of the collagenous fibrils in cartilage, which may offer a powerful tool to evaluate structure-modifying therapeutic approaches in knee diseases.

REFERENCES

1. Sophia Fox AJ, Bedi A, Rodeo SA. The basic science of articular cartilage: structure, composition, and function. Sports Health 2009;1: 461–468.
2. Hunziker E, Quinn T, Häuselmann H-J. Quantitative structural organization of normal adult human articular cartilage. Osteoarthr Cartil 2002;10:564–572.
3. Goldring MB, Goldring SR. Articular cartilage and subchondral bone in the pathogenesis of osteoarthritis. Ann N Y Acad Sci 2010;1192: 230–237.
4. Pritzker K, Gay S, Jimenez S, Ostergaard K, Pelletier J-P, Revell P, Salter D, Van den Berg W. Osteoarthritis cartilage histopathology: grading and staging. Osteoarthr Cartil 2006;14:13–29.
5. Burstein D, Bashir A, Gray ML. MRI techniques in early stages of cartilage disease. Invest Radiol 2000;35:622–638.
6. Mosher TJ, Dardzinski BJ. Cartilage MRI T2 relaxation time mapping: overview and applications. New York: Thieme Medical Publishers; 2004.
7. Jordan CD, Saranathan M, Bangerter NK, Hargreaves BA, Gold GE. Musculoskeletal MRI at 3.0 T and 7.0 T: a comparison of relaxation times and image contrast. Eur J Radiol 2013;82:734–739.
8. Nieminen MT, Rieppo J, Töyräs J, Hakumäki JM, Silvennoinen J, Hyttinen MM, Helminen HJ, Jurvelin JS. T2 relaxation reveals spatial collagen architecture in articular cartilage: a comparative quantitative MRI and polarized light microscopic study. Magn Reson Med 2001; 46:487–493.
9. Reddy R, Insko EK, Noyszewski EA, Dandora R, Kneeland JB, Leigh JS. Sodium MRI of human articular cartilage in vivo. Magn Reson Med 1998;39:697–701.
10. Filidoro L, Dietrich O, Weber J, Rauch E, Oerther T, Wick M, Reiser M, Glaser C. High-resolution diffusion tensor imaging of human patellar cartilage: Feasibility and preliminary findings. Magn Reson Med 2005;53:993–998.
11. Staroswiecki E, Granlund KL, Alley MT, Gold GE, Hargreaves BA. Simultaneous estimation of T2 and apparent diffusion coefficient in human articular cartilage in vivo with a modified three-dimensional double echo steady state (DESS) sequence at 3 T. Magn Reson Med 2012;67:1086–1096.
12. Dibb R, Liu C. Joint eigenvector estimation from mutually anisotropic tensors improves susceptibility tensor imaging of the brain, kidney, and heart. Magn Reson Med 2017;77:2331–2346.
13. Wei H, Xie L, Dibb R, Li W, Decker K, Zhang Y, Johnson GA, Liu C. Imaging whole-brain cytoarchitecture of mouse with MRI-based quantitative susceptibility mapping. NeuroImage 2016;137:107–115.
14. Nissi MJ, Tóth F, Wang L, Carlson CS, Ellermann JM. Improved visualization of cartilage canals using quantitative susceptibility mapping. PloS One 2015;10:e0132167.
15. Dibb R, Qi Y, Liu C. Magnetic susceptibility anisotropy of myocardium imaged by cardiovascular magnetic resonance reflects the anisotropy of myocardial filament α-helix polypeptide bonds. J Cardiovasc Magn Reson 2015;17:60.
16. Wang L, Nissi MJ, Toth F, Johnson CP, Garwood M, Carlson CS, Ellermann J. Quantitative susceptibility mapping detects abnormalities in cartilage canals in a goat model of preclinical osteochondritis dissecans. Magn Reson Med 2017;77:1276–1283.
17. Dimov AV, Liu Z, Spincemaille P, Prince MR, Du J, Wang Y. Bone quantitative susceptibility mapping using a chemical species–specific R2* signal model with ultrashort and conventional echo data. Magn Reson Med 2017. doi: 10.1002/mrm.26648.
18. Xie L, Dibb R, Cofer GP, Li W, Nicholls PJ, Johnson GA, Liu C. Susceptibility tensor imaging of the kidney and its microstructural underpinnings. Magn Reson Med 2015;73:1270–1281.
19. Wei H, Dibb R, Decker K, Wang N, Zhang Y, Zong X, Lin W, Nissman DB, Liu C. Investigating magnetic susceptibility of human knee joint at 7 Tesla. Magn Reson Med 2017. doi: 10.1002/mrm.26596.
20. Wei H, Wang B, Zong X, Lin W, Wang N, Liu C. Imaging Magnetic Susceptibility of the Human Knee Joint at 3 and 7 Tesla. In Proceedings of the 23rd Annual Meeting of ISMRM, Toronto, ON, Canada, 2015. p. 288.
21. Haacke EM, Xu Y, Cheng YCN, Reichenbach JR. Susceptibility weighted imaging (SWI). Magn Reson Med 2004;52:612–618.
22. Liu C, Li W, Johnson GA, Wu B. High-field (9.4 T) MRI of brain dysmyelination by quantitative mapping of magnetic susceptibility. Neuroimage 2011;56:930–938.
23. Wei H, Zhang Y, Gibbs E, Chen NK, Wang N, Liu C. Joint 2D and 3D phase processing for quantitative susceptibility mapping: application to 2D echo-planar imaging. NMR Biomed 2017;30.
24. Liu C, Li W, Tong KA, Yeom KW, Kuzminski S. Susceptibility-weighted imaging and quantitative susceptibility mapping in the brain. J Magn Reson Imaging 2014;42:23–41.
25. Liu C, Wei H, Gong N-J, Cronin M, Dibb R, Decker K. Quantitative susceptibility mapping: contrast mechanisms and clinical applications. Tomography 2015;1:3–17.
26. Aggarwal M, Kageyama Y, Li X, Van Zijl PC. B0-orientation dependent magnetic susceptibility-induced white matter contrast in the human brainstem at 11.7 T. Magn Reson Med 2016;75:2455–2463.
27. Li W, Liu C, Duong TQ, Zijl P, Li X. Susceptibility tensor imaging (STI) of the brain. NMR Biomed 2017;30.
28. Li X, Vikram DS, Lim IAL, Jones CK, Farrell JA, van Zijl PC. Mapping magnetic susceptibility anisotropies of white matter in vivo in the human brain at 7T. Neuroimage 2012;62:314–330.
29. Li X, Zijl P. Mean magnetic susceptibility regularized susceptibility tensor imaging (MMSR-STI) for estimating orientations of white matter fibers in human brain. Magn Reson Med 2014;72:610–619.
30. Liu C. Susceptibility tensor imaging. Magn Reson Med 2010;63:1471–1477.
31. Wharton S, Bowtell R. Fiber orientation-dependent white matter contrast in gradient echo MRI. Proc Natl Acad Sci U S A 2012;109: 18559–18564.
32. Wisnieff C, Liu T, Spincemaille P, Wang S, Zhou D, Wang Y. Magnetic susceptibility anisotropy: cylindrical symmetry from macroscopically ordered anisotropic molecules and accuracy of MRI measurements using few orientations. Neuroimage 2013;70:363–376.
33. Bilgic B, Xie L, Dibb R, Langkammer C, Mutluay A, Ye H, Polimeni JR, Augustinack J, Liu C, Wald LL. Rapid multi-orientation quantitative susceptibility mapping. NeuroImage 2016;125:1131–1141.
34. Liu C, Li W, Wu B, Jiang Y, Johnson GA. 3D fiber tractography with susceptibility tensor imaging. Neuroimage 2012;59:1290–1298.
35. Dibb R, Xie L, Wei H, Liu C. Magnetic susceptibility anisotropy outside the central nervous system. NMR Biomed 2017;30.
36. Johnson GA, Cofer GP, Gewalt SL, Hedlund LW. Morphologic phenotyping with MR microscopy: the visible mouse 1. Radiology 2002; 222:789–793.
37. Li W, Wu B, Avram AV, Liu C. Magnetic susceptibility anisotropy of human brain in vivo and its molecular underpinnings. Neuroimage 2012;59:2088–2097.
38. Wu B, Li W, Guidon A, Liu C. Whole brain susceptibility mapping using compressed sensing. Magn Reson Med 2012;67:137–147.
39. Basser PJ, Pierpaoli C. Microstructural and physiological features of tissues elucidated by quantitative-diffusion-tensor MRI. J Magn Reson 2011;213:560–570.
40. Mori S, Kaufmann WE, Davatzikos C, Stieltjes B, Amodei L, Fredericksen K, Pearlson GD, Melhem ER, Solaiyappan M, Raymond GV. Imaging cortical association tracts in the human brain using diffusion-tensor-based axonal tracking. Magn Reson Med 2002;47: 215–223.
41. Drake B, Prater C, Weisenhorn A, Gould S, Albrecht T. Imaging crystals, polymers, and processes in water with the atomic force microscope. Science 1989;243:1586.
42. Sawadkar P, Alexander S, Tolk M, Wong J, McGrouther D, Bozec L, Mudera V. Development of a surgically optimized graft insertion suture technique to accommodate a tissue-engineered tendon in vivo. Biores Open Access 2013;2:327–335.
43. Avci R, Schweitzer M, Boyd RD, Wittmeyer J, Steele A, Toporski J, Beech I, Arce FT, Spangler B, Cole KM. Comparison of antibody–antigen interactions on collagen measured by conventional immunological techniques and atomic force microscopy. Langmuir 2004;20:11053–11063.
44. Schmitz N, Laverty S, Kraus V, Aigner T. Basic methods in histopathology of joint tissues. Osteoarthr Cartil 2010;18:S113–S116.
45. Shoulders MD, Raines RT. Collagen structure and stability. Annu Rev Biochem 2009;78:929–958.
46. Holmes DF, Kadler KE. The 10 + 4 microfibril structure of thin cartilage fibrils. Proc Natl Acad Sci U S A 2006;103:17249–17254.
47. Xia Y, Momot K, editors. Biophysics and biochemistry of cartilage by NMR and MRI. London: Royal Society of Chemistry; 2016.
48. Lewis PN, Pinali C, Young RD, Meek KM, Quantock AJ, Knupp C. Structural interactions between collagen and proteoglycans are elucidated by three-dimensional electron tomography of bovine cornea. Structure 2010;18:239–245.

49. Worcester D. Structural origins of diamagnetic anisotropy in proteins. Proc Natl Acad Sci U S A 1978;75:5475–5477.
50. Torbet J, Ronzière M-C. Magnetic alignment of collagen during self-assembly. Biochem J 1984;219:1057–1059.
51. Liu C, Li W. Imaging neural architecture of the brain based on its multipole magnetic response. Neuroimage 2013;67:193–202.
52. McGinley JV, Ristic M, Young IR. A permanent MRI magnet for magic angle imaging having its field parallel to the poles. J Magn Reson 2016;271:60–67.

SUPPORTING INFORMATION

Additional Supporting Information may be found in the online version of this article.

Fig. S1. STI orientation sampling. The unit vectors of 12 object orientations are shown for an ex vivo cartilage experiment.
Fig. S2. 3D visualization of tensor fields derived from DTI (**a**) and STI (**b**). The multi-layer cartilage structure is clearly depicted in STI by the collagen fibril orientation at different depths within the cartilage.
Fig. S3. Representative images of susceptibility anisotropy (**a**), color-coded susceptibility anisotropy (**b**), and 3D fiber tracts (**c, d**) of another cartilage specimen. Similar results were observed as shown in Figs. 3–5. Twelve image orientations were acquired for this specimen.
Fig. S4. Investigating the effects of diffusion time for detecting diffusion anisotropy of collagen fibrils. Representative diffusion weighted (DW) images, MD, FA, and color-coded diffusion anisotropy with diffusion time of (**a**) 8 ms and (**b**) 16 ms. DTI fails to detect the orientation of collagen fibril in the cartilage although with longer diffusion time up to 16 ms.